Ultrasonics 94 (2019) 158–168

Contents lists available at ScienceDirect

Ultrasonics

journal homepage: www.elsevier.com/locate/ultras

Backward waves and energy fluxes excited in acoustic medium with an immersed plate

E.V. Glushkov*, N.V. Glushkova, O.A. Miakisheva

Institute for Mathematics, Mechanics and Informatics, Kuban State University, Krasnodar, Russia

ARTICLE INFO

Keywords:
Immersed elastic plate
Ultrasonic sounding
Integral and asymptotic representations
Backward modes
Resonance transmission
Source energy partition

ABSTRACT

Explicit integral representations for the wave fields generated by air-coupled or underwater transducers in an acoustic medium with a submerged elastic (metallic or laminate composite) plate are obtained in the form of path Fourier integrals. Together with the far-field asymptotics for the incident, reflected, transmitted and guided waves that were derived from those integrals, they proved to be a convenient tool for the in-depth study of wave phenomena inherent in such acoustic-elastic structures. The present paper is focused on the non-conventional properties of backward leaky waves such as the increased wave energy transfer through the plate due to the increasing occurrence of energy vortices impeding lateral outflow of wave energy. The transformation of classical Lamb waves into leaky guided waves due to a fluid loading, especially in the backward wave range, the energy properties of those waves and the appearing traveling Scholter-Stoneley waves as well as source energy partition among the reflected, transmitted and guided waves are also numerically illustrated and discussed.

1. Introduction

The interaction of sound and ultrasound waves with an elastic plate immersed in acoustic medium (liquid or gas) is a classical problem of structural acoustics. It relates to numerous technical applications ranging from vibration isolation, noise control and acoustic stealth to ultrasonic non-destructive evaluation (NDE). An important specific motivation for the present research is a study of wave processes underlying the work of acoustic microscopes and ultrasonic underwater and air-coupled transducers [1] (Fig. 1). The latter are often used as a cheaper alternative to the laser Doppler vibrometry. Guided waves (GWs) generated in the plate by the ultrasonic beams have been increasingly used for long range ultrasonic NDE within the Structural Health Monitoring concept [2,3]. The development of adequate and efficient mathematical models facilitates the choice of optimal parameters and operating modes for such devices and technologies.

The analysis of incident plane-wave reflection from and transmission through a laminate plate is now a fairly standard procedure [4]. The classical problem of wave interaction with immersed thin-wall structures is well studied on the basis of ray and modal analysis techniques [5–8]. These methods allow one to analyze the reflection and transmission of acoustic beams and to obtain the dispersion characteristics of GWs propagating over the plate. However, it is still complicated to simulate wave processes in such fluid-loaded structures with a strict accounting for the wave source, i.e., via the solution of a coupled source-structure boundary value problem (BVP). Finite-element (FEM) packages are ample for such simulation [9], but their use is often too expensive, and the total FEM results are not as physically clear as analytically based expansions in terms of bulk and guided waves.

A thorough review of various semi-analytical methods can be found in Ref. [10]. The advantages and limitations of such approaches as the use of Huygens' principle [11] and superimposing of Gaussian beam solution [12,13] are discussed in comparison with the distributed point source method (DPSM) [14]. The DPSM avoids the most of those limitations and does not require any far-field approximation. However, being a special case of the boundary element method, it is based on the wave field representation in terms of fundamental solutions for unbounded homogeneous acoustic and elastic media. Therefore, its application assumes the distribution of such basis functions (boundary elements) over all boundaries and interfaces of the structure considered (e.g., Fig. 1 in Ref. [10]).

A drastic reduction in the number of basis functions (distributed sources) can be achieved with the laminate element method (LEM) [15], which is based on the use of fundamental solutions (Green's functions) of the laminate structure as a whole. Such basis functions automatically satisfy the conditions at all plane-parallel boundaries and interfaces, so that only the conditions at the local surfaces of the source and obstacles are to be approximated. Specifically, to simulate the

* Corresponding author.
E-mail address: evg@math.kubsu.ru (E.V. Glushkov).

https://doi.org/10.1016/j.ultras.2018.10.001
Received 21 February 2018; Received in revised form 30 September 2018; Accepted 2 October 2018
Available online 04 October 2018

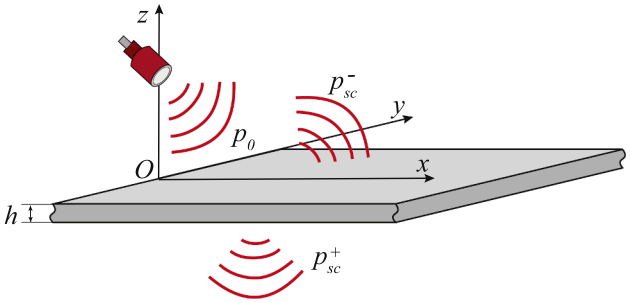

Fig. 1. Ultrasonic sounding, geometry of the problem.

source generated waves in the acoustic-elastic structures considered, it is sufficient to distribute the laminate elements only along the emitter. There is no need to distribute them along the plate's parallel surfaces and interfaces that extend to infinity, and, consequently, there is no problem of their correct truncation.

The use of Green's function based integral representations of wave fields for immersed plates is a known method (e.g., [16]). In no small measure, the present research has been induced by S. Banerjee [10], who encouraged us to implement the LEM technique to the source-sounded fluid-loaded laminate plates. The key stage of LEM implementation is the elaboration of efficient algorithms for Green's function calculation. We have been developing such algorithms for vertically inhomogeneous (stratified) elastic half-spaces subjected to surface loading. The inhomogeneity may be both piecewise constant (laminates) [15] and functionally gradient [17], including fluid sublayers as a particular case of elastic medium with zero shear wave velocity. The main idea of the present approach is to use these algorithms that we already have in hand as a basis for the Green's function calculation for the immersed elastic waveguides. The incorporation of the Green's matrix K for the underlying elastic half-space into the representation for the Green's function for a submerged plate requires minimal analytic effort, as described in Section 3 below. This approach opens the possibility to simulate the source-generated non-contact probing of various waveguide structures, including anisotropic laminate composites [18] and piezoelectric [19] guides.

In the present study, the numerical analysis is limited to the classical case of isotropic plate sounded by a normally oriented transducer, which is enough for the objectives of the research. However, the mathematical framework is given in the general form to be easily used with more complex structures and tilted or concave emitters.

The Green's functions are obtained in the explicit form of inverse path Fourier integrals. While their numerical integration in the near field is still a rather time-consuming procedure, the asymptotics for the incident, reflected, transmitted and leaky guided waves derived from those integrals provide low-cost and physically evident analytical expressions for the evaluation of source excited waves in the far field. The explicit solutions have also been used to derive compact integral representations for the wave energy emitted from the source and its partition among the bulk and guided waves. Moreover, they make it possible to visualize time-averaged energy fluxes from the source to infinity by tracing the energy streamlines specified by the vector field of the Umov-Poynting vectors of energy flux intensity [20].

In the present paper, first, we give a general description of the mathematical and computational model developed. Then its abilities are illustrated by a few validating numerical examples. Here we focus on the effect of increased acoustic energy transfer through the plate [21] that occurs at the plate thickness resonance frequencies and in the backward mode range. The numerical results obtained are compared with the experimental and FEM results [22]. The analysis of the structure of wave energy streamlines in resonance and non-resonance cases complements the understanding of the mechanism of resonance transmission.

Independent interest is the backward leaky wave phenomenon. In spite of the well-known studies of the Lamb mode non-propagating branches and complex dispersion curve transformation under liquid loading [7,23], seemingly unusual wave energy effects still occur in this range that require an explanation [24]. To clarify those effects, the transformation of the classical Lamb waves, including backward modes, into guided leaky waves with fluid loading, and the peculiarities of wave energy transportation along the plate, especially in the backward wave range, are also analyzed and discussed.

2. Mathematical framework

Let us consider a steady-state time-harmonic oscillation $\mathbf{u}(\mathbf{x})e^{-i\omega t}$ of an elastic plate of thickness h submerged in acoustic environment. In Cartesian coordinates $\mathbf{x} = (x, y, z)$, the plate occupies the volume D: $-\infty < x, y < \infty$, $-h \leqslant z \leqslant 0$ (Fig. 1). Most generally, it may be a laminate composite plate, which displacement amplitude $\mathbf{u} = (u_x, u_y, u_z)$ obeys the full set of linear elastodynamics equations for anisotropic media [18,25]. In simpler models, the plate's material is isotropic, governed by the Navier-Lamé equation

$$(\lambda + \mu)\nabla \mathrm{div}\mathbf{u} + \mu\Delta\mathbf{u} + \rho\omega^2\mathbf{u} = 0, \quad \mathbf{x} \in D. \tag{1}$$

Here λ and μ are Lamé elastic moduli, ρ is density, $\omega = 2\pi f$ is angular frequency, and f is frequency; the time-harmonic factor $e^{-i\omega t}$ is conventionally omitted.

A source located in the upper acoustic half-space $z > 0$ or attached to its surface $z = 0$ generates the pressure field

$$p(\mathbf{x}) = \begin{cases} p_0(\mathbf{x}) + p_{sc}^-(\mathbf{x}), & z \geqslant 0 \\ p_{sc}^+(\mathbf{x}), & z \leqslant -h \end{cases}. \tag{2}$$

in the acoustic medium and the displacement field $\mathbf{u}(\mathbf{x})$ in the plate. Here p_0 is the direct source field while p_{sc}^- and p_{sc}^+ stand for the reflected and transmitted scattered fields, respectively.

The wave fields $\mathbf{u}(\mathbf{x})$ and $p(\mathbf{x})$ in the plate and environment are coupled by the conditions of continuity of the normal displacement and stress components at the plate-fluid interfaces $z = 0$ and $z = -h$. In view of the relation $\mathbf{u} = \nabla p/(\rho_0\omega^2)$ between the displacement and pressure complex amplitudes in fluid, the coupling boundary conditions take the form

$$\begin{aligned} &u_z = \tfrac{1}{\rho_0\omega^2}\tfrac{\partial p}{\partial z}, \\ &\sigma_z = -p, \ \ \tau_{xz} = \tau_{yz} = 0 \end{aligned} \qquad \text{at } z = 0 \text{ and } z = -h. \tag{3}$$

Here ρ_0 is the density of acoustic fluid, and the components of the stress vector $\boldsymbol{\tau} = (\tau_{xz}, \tau_{yz}, \sigma_z)$ are expressed via the displacement components in accordance with Hooke's law [25]. Conditions (3) also take into account the absence of tangential tensions and the opposite of signs of the normal stress and acoustic pressure load at the fluid-solid interfaces. To ensure correct radiation at infinity, we use the principle of limiting absorption [26].

The wave source is modeled by a given distribution $q_0(\mathbf{x})$ of some driven force F over the surface S of the radiating element. The pressure and displacement fields generated by this distributed force can be represented as the integral over S of the *pressure and displacement Green's functions* $g(\mathbf{x}, \boldsymbol{\xi})$ and $\mathbf{g}_u(\mathbf{x}, \boldsymbol{\xi})$ multiplied by the distribution $q_0(\boldsymbol{\xi})$:

$$p(\mathbf{x}) = \iint_S g\left(\mathbf{x}, \boldsymbol{\xi}\right) q_0(\boldsymbol{\xi}) d\boldsymbol{\xi} \approx \sum_j A_j g\left(\mathbf{x}, \boldsymbol{\xi}_j\right) q_0(\boldsymbol{\xi}_j), \ \ \mathbf{x} \notin S, \ \ \mathbf{x} \notin D, \tag{4}$$

$$\mathbf{u}(\mathbf{x}) = \iint_S \mathbf{g}_u\left(\mathbf{x}, \boldsymbol{\xi}\right) q_0(\boldsymbol{\xi}) d\boldsymbol{\xi} \approx \sum_j A_j \mathbf{g}_u\left(\mathbf{x}, \boldsymbol{\xi}_j\right) q_0(\boldsymbol{\xi}_j), \quad \mathbf{x} \in D. \tag{5}$$

Here $\boldsymbol{\xi}_j \in S$ are source points distributed over S, and A_j are weight coefficients of a cubature formula used for the numerical integration.

Not infrequently, the shape of the area S (e.g., of a circular emitter) and the law of the distribution q_0 chosen in the model enable the analytical integration in Eqs. (4) and (5), eliminating the need for numerical approximation.

In view of the connection between the displacement and pressure fields in an acoustic medium, the displacement Green's function can be extended onto the whole space by the relation $\mathbf{g}_u = \nabla g/(\rho_0\omega^2)$ for $z > 0$ and $z < -h$.

3. Green's functions

Both the pressure and displacement Green's functions $g(\mathbf{x}, \boldsymbol{\xi})$ and $\mathbf{g}_u(\mathbf{x}, \boldsymbol{\xi})$ are derived as the fundamental (point-source) solution to the coupled BVP for the monopole source located at a point $\boldsymbol{\xi} = (\xi, \eta, \zeta)$ in the upper half-space ($\zeta \geqslant 0$).

The pressure Green's function, which is determined in the acoustic half-spaces $z \geqslant 0$ and $z \leqslant -h$, obeys the Helmholtz equation

$$\Delta g + \varkappa_0^2 g = \delta(\mathbf{x}-\boldsymbol{\xi}). \tag{6}$$

Here $\varkappa_0 = \omega/c_0$ is the wavenumber of bulk waves in the acoustic medium, c_0 is their phase velocity.

The Green's functions satisfy the same boundary conditions as Eq. (3) with p replaced by g and $\mathbf{u}$ replaced by $\mathbf{g}_u$. In the plate domain D, the latter is governed by the same elastodynamic equations as $\mathbf{u}$ (Eq. (1) in the isotropic case).

Same as in Eq. (2), the pressure Green's function g can be represented above the plate by a sum of the direct and scattered fields: $g = g_0 + g_{sc}^-$, where

$$g_0\left(\mathbf{x}-\boldsymbol{\xi}\right) = -\frac{1}{4\pi}\frac{e^{i\varkappa_0 R}}{R}, \quad R = \left|\mathbf{x}-\boldsymbol{\xi}\right| \tag{7}$$

is the classical fundamental solution to Eq. (6). It describes a spherical bulk wave generated by the monopole source in a homogeneous space. As for the scattered parts $g_{sc}^{\pm}$ and the displacement Green's function $\mathbf{g}_u$, their explicit integral representations are derived via the application of the Fourier transform $\mathscr{F}_{xy}$ with respect to the horizontal coordinates x and y, which reduces the BVP equations to the system of ordinary differential equations. The Fourier symbols $G = \mathscr{F}_{xy}[g]$and $\mathbf{G}_u = \mathscr{F}_{xy}[\mathbf{g}_u]$ are derived analytically while the corresponding Green's functions are obtained as the inverse Fourier integrals:

$$g\left(\mathbf{x}, \boldsymbol{\xi}\right) = \mathscr{F}_{xy}^{-1}[G] = \frac{1}{(2\pi)^2}\int_{\Gamma_1}\int_{\Gamma_2} G\left(\alpha_1, \alpha_2, z;\boldsymbol{\xi}\right)e^{-i(\alpha_1 x+\alpha_2 y)}d\alpha_1 d\alpha_2, \tag{8}$$

and similarly for $\mathbf{g}_u$. The integration paths Γ_1 and Γ_2 go along the real axes in the complex planes α_1 and α_2, deviating from them to round the real poles of the integrands in accordance with the principle of limiting absorption (see Refs. [18,27] for details).

In view of the splitting $g = g_0 + g_{sc}^-$,

$$G(\alpha_1, \alpha_2, z;\boldsymbol{\xi}) = [G_0(\alpha, z-\zeta) + G_{sc}^-(\alpha_1, \alpha_2, z;\zeta)]e^{i(\alpha_1\xi+\alpha_2\eta)}, \quad z \geqslant 0, \tag{9}$$

where

$$G_0(\alpha, z) = -e^{-\sigma_0|z|}/(2\sigma_0), \quad G_{sc}^-(\alpha, z;\zeta) = c_1(\zeta)e^{-\sigma_0 z},$$
$$\alpha = \sqrt{\alpha_1^2+\alpha_2^2}, \quad \sigma_0 = \sqrt{\alpha^2-\varkappa_0^2}, \quad \mathrm{Re}\,\sigma_0 \geqslant 0, \quad \mathrm{Im}\,\sigma_0 \leqslant 0, \tag{10}$$

and the unknown coefficient c_1 is to be obtained from the Fourier transformed coupling boundary conditions at $z = 0$.

The function $\mathbf{G}_u$ is obtained on the basis of the existing algorithms of Green's matrix calculation for a stratified elastic half-space $z \leqslant 0$ subjected to a surface load $\boldsymbol{\tau} = \mathbf{q}$ (e.g., [15,18]).

With any dependence of the half-space elastic moduli and density on the depth z (including the degeneration of elastic solid into the acoustic fluid as the shear modulus $\mu \to 0$ and Poisson's ratio $\nu \to 0.5$, which is required for $z \leqslant -h$ in the case), the half-space solution in the Fourier transform domain takes the form

$$\mathbf{U}(\alpha_1, \alpha_2, z) = K(\alpha_1, \alpha_2, z)\mathbf{Q}(\alpha_1, \alpha_2), \quad z \leqslant 0, \tag{11}$$

where $\mathbf{U} = \mathscr{F}_{xy}[\mathbf{u}]$, $\mathbf{Q} = \mathscr{F}_{xy}[\mathbf{q}]$ and $K = \mathscr{F}_{xy}[k]$ are the Fourier symbols of the displacement $\mathbf{u}(\mathbf{x})$, surface load $\mathbf{q}(x, y)$ and 3×3 Green's matrix $k(\mathbf{x})$ of the elastic-fluid half-space $z \leqslant 0$. The matrix K can be written as the ratio of the matrix numerator $\widehat{K}$ and the denominator . The latter yields the characteristic (dispersion) equation $\Delta(\alpha_1, \alpha_2, \omega) = 0$ for the GWs excited in the half-space without fluid loading.

With a fluid loading, the tangential components of the load vector are zero: $\mathbf{q} = (0, 0, q)$, so that only the third column $\mathbf{K}_3$ of the matrix K works in Eq. (11): $\mathbf{U} = \mathbf{K}_3 Q$. Wherein, the Fourier symbol Q of the stress q induced at the interface $z = 0$ by the field p_0 emitted by the point source located at the distance $\zeta = d$ from the plate is derived from the Fourier transformed boundary conditions $g = -q$ and $\partial g/\partial z = \rho_0\omega^2 u_z$ at $z = 0$ with accounting for Eqs. (9)–(11):

$$Q = (\Delta/\Delta_0)e^{-\sigma_0 d}e^{i(\alpha_1\xi+\alpha_2\eta)},$$
$$G_{sc}^- = -(\sigma_0\Delta + \rho_0\omega^2\widehat{K}_{33}(\alpha_1, \alpha_2, 0))/(2\sigma_0\Delta_0)e^{-\sigma_0(z+d)},$$
$$\Delta_0 = \sigma_0\Delta - \rho_0\omega^2\widehat{K}_{33}(\alpha_1, \alpha_2, 0).$$

Function Δ_0 is the common denominator of the pressure Green's function G and the displacement Green's function

$$\mathbf{G}_u(\alpha_1, \alpha_2, z;\boldsymbol{\xi}) = \mathbf{K}_3 Q = (\widehat{\mathbf{K}}_3/\Delta_0)e^{-\sigma_0 d+i(\alpha_1\xi+\alpha_2\eta)}, \quad z \leqslant 0. \tag{12}$$

Since the matrix K is defined in the whole lower half-space $z \leqslant 0$, including the fluid half-space $z \leqslant h$, the lower part of the pressure Green's function can be derived from Eq. (12) in the form

$$G = G_{sc}^+ = -\rho_0\omega^2\sigma_0\widehat{K}_{33}(\alpha_1, \alpha_2, z)e^{-\sigma_0 d}/\Delta_0, \quad z \leqslant -h. \tag{13}$$

It is worthy to note that the denominator of $\mathbf{K}_3$ is reduced here with the same function Δ in the numerator of Q, so that there appears a new characteristic equation for the GWs in the fluid-loaded half-space:

$$\Delta_0(\alpha_1, \alpha_2, \omega) = 0 \tag{14}$$

instead of the equation $\Delta = 0$ for the half-space in the vacuum. It is evident that $\Delta_0 \to \sigma_0\Delta$ as $\rho_0 \to 0$, i.e., as the acoustic loading becomes impalpable. In the isotropic case, $\Delta_0 = \Delta_0(\alpha, \omega)$ depends only on the radial variable α in the plane (α_1, α_2) (the polar coordinates are introduced in Eq. (14) below). The roots of Eq. (13) ζ_n are the wavenumbers of GWs propagating along the plate. With an isotropic plate, they are also independent of the angular variable γ.

A comprehensive description of the calculation algorithms for the K matrix and, consequently, for the Green's functions $G_{sc}^{\pm}$ and $\mathbf{G}_u$, in the case of multilayer isotropic and anisotropic elastic waveguides are available in Refs. [15,18], respectively. Analytic representations for the particular case of an immersed homogeneous isotropic plate are given in Appendix A.

4. Guided and bulk waves

Being the exact solutions to the point-source BVPs, the Green's functions expressed through the path Fourier integrals of form (8) contain precise quantitative information about the waves of all types excited by the source. In the isotropic case, there is no need in numerical integration of such double-fold path integrals, since in the polar coordinates

$$\begin{array}{ll} x-\xi = r\cos\varphi, \ y-\eta = r\sin\varphi & \alpha_1 = \alpha\cos\gamma, \ \alpha_2 = \alpha\sin\gamma \\ r = \sqrt{(x-\xi)^2+(y-\eta)^2} \quad , & \alpha = \sqrt{\alpha_1^2+\alpha_2^2} \\ 0 \leqslant \varphi < 2\pi & 0 \leqslant \gamma < 2\pi \end{array} \tag{15}$$

they can be reduced to onefold integrals over α, which numerical integration in the near field becomes quite acceptable. For example, for the function G of form (9), Eq. (8) can be reduced to the form

$$g\left(\mathbf{x},\,\boldsymbol{\xi}\right)=g_0\left(\mathbf{x}-\boldsymbol{\xi}\right)+\frac{1}{\pi}\int_{\Gamma}G_{sc}^{-}\left(\alpha,\,z;\zeta\right)H_0^{(1)}\left(\alpha r\right)\alpha d\alpha, \tag{16}$$

where Γ is the so-called unfold integration contour [18,27], and $H_0^{(1)}$ is the Hankel function of the first kind and zero order.

In the far field $\varkappa R \gg 1$ ($\varkappa$ is a characteristic wavenumber), the oscillation in the integrands increases, and asymptotic evaluation becomes more profitable. The stationary phase points yield the asymptotic expressions for the transmitted and reflected spherical acoustic waves $g_{sc}^{\pm}$ [28] while the residues from the poles $\alpha=\zeta_n$ of the integrands $\mathbf{G}_u$ and G depict, in the isotropic case, axially symmetric cylindrical GWs propagating over the plate and in the adjacent acoustic environment. Inside the plate

$$\mathbf{u}_c\left(r,\,z\right)\sim\sum_n\mathbf{b}_n(z)e^{i\zeta_n r}/\sqrt{\zeta_n r},\quad \zeta_n r\to\infty$$
$$\mathbf{b}_n=i\widehat{\mathbf{K}}_3(\zeta_n,\,z)e^{-i\sigma_{0,n}\zeta}/(2\Delta_0'(\zeta_n)),\quad \sigma_{0,n}=\sqrt{\zeta_n^2-\varkappa_0^2}, \tag{17}$$

where $\mathbf{u}_c=(u_r,\,u_z)$ denotes $\mathbf{g}_u$ written in the cylindrical coordinates $(r,\,\varphi,\,z)$ in the case of axial symmetry ($u_\varphi\equiv 0$); Δ_0' is the derivative of Δ_0 with respect to α.

In the anisotropic case, the GW asymptotics cannot be obtained by simple substitution of the residues of $\widehat{\mathbf{K}}_3/\Delta_0$ into Eq. (17). Nevertheless, the residues from the angular dependent poles $\alpha=\zeta_n(\gamma)$ also yield the far-field asymptotics of quasi-cylindrical GWs. Its derivation is described in detail in Ref. [18].

5. Traveling and leaky waves

In GW asymptotics (17), the dependence of the amplitude factors $\mathbf{b}_n$ on z coincides, up to constant coefficients, with the eigenforms of the corresponding normal modes obtained using the modal analysis technique. Moreover, the exponentials $e^{-\sigma_{0,n}d}$ uniquely specify the GW amplitudes, depending on the distance d from the point source to the plate. The terms of Eq. (17) associated with the real roots (wavenumbers) ζ_n are classical traveling waves propagating without exponential decay while complex ζ_n yield evanescent waves. They propagate with the phase velocities $c_n=\omega/\mathrm{Re}\,\zeta_n$ and attenuation factors $e^{-|\mathrm{Im}\,\zeta_n|r}$ controlled by the imaginary parts of the poles. With a free homogeneous elastic plate, pure real poles yield classical Lamb waves (Fig. 2a); A_n and S_n conventionally denote the branches of antisymmetric and symmetric fundamental ($n=0$) and higher ($n=1,\,2,\,3,\,\ldots$) modes. Fluid loading ($\rho_0\neq 0$ in Δ_0) causes a slight shift of the real poles into the complex plane (Fig. 2b) reflecting the appearance of exponential attenuation due to the leakage of wave energy into the environment.

In accordance with the general law of GW propagation in internal waveguides, the leakage occurs when the GW phase velocity is greater than the bulk wave velocity in the environment ($c_n>c_0$). This takes place for the branches ζ_n, which real parts lie below the straight line $\varkappa_0=\omega/c_0$ marked in Fig. 2b, c by bold dots ($\mathrm{Re}\zeta_n(\omega)<\varkappa_0(\omega)$). One can see that almost all branches A_n and S_n meet this condition, and, in the immersed plate, they become leaky Lamb waves, except the small part of A_0 mode in the low-frequency range $0<\omega<0.44$ (Fig. 2c). Besides them, two new real branches A and S appear with a fluid loading that yield the Scholte-Stoneley guided waves [29,30]. Their pure real dispersion-curve branches go very close to the straight line $\varkappa_0=\omega/c_0$, i.e., these waves propagate almost with the sound velocity in the liquid, still not coinciding with it (Fig. 2c).

The numerical results here and in some other figures below are presented in the dimensionless form obtained by normalizing all dimensional parameters to the three basic units: the unit of length $l_u=h$, the unit of velocity $v_u=c_s$, and the unit of density $\rho_u=\rho$ as well as to all other units expressed in terms of these basic values. For example, the unit of frequency is $f_u=v_u/l_u=h/c_s$, the unit of stresses, pressure and elastic modules is $\tau_u=\rho_u v_u^2=\rho c_s^2$, the unit of pressure frequency spectra is $p_u=\tau_u/f_u=\rho c_s h$, and so on. With such choice, the dimensionless angular frequency $\omega=2\pi f h/c_s$, where f is dimensional frequency. To obtain dimensional results for a particular specimen from the dimensionless results applicable for a variety of samples, it is necessary to specify the dimensionless input parameters corresponding to the structure under study before the numerical calculations, and multiply the obtained dimensionless results by the basic and following from them units.

To be comparable with the results of work [22], we have taken the following dimensionless input parameters: $c_p=1.847$, $c_s=1$, $\rho=1$, $h=1$, $c_0=0.474$, and $\rho_0=0.125$. They correspond to the dimensional parameters of a steel plate of thickness $h=6.05$ mm, density $\rho=8000\,\mathrm{kg/m^3}$, P-wave velocity $c_p=5780$ m/s and S-wave velocity $c_s=3130$ m/s. The density of the surrounding liquid is $\rho_0=1000\,\mathrm{kg/m^3}$, and the sound velocity is $c_0=1485$ m/s. Since in Ref. [22] the magnitude and distribution of the transducer force are not specified, we simulate the source by the dimensionless distribution $q_0=1$ given in a circular area S of radius a. For the transducer of radius 30 mm, dimensionless $a=4.959$.

The branch S_1 in Fig. 2a has a characteristic bend in the range $5.42<\omega<5.81$ with a negative slope of the tangent indicating the appearance of the so-called backward mode S_1^*. At the left end of this range, the tangent is vertical yielding the mode with zero group velocity $v_n=d\omega/d\zeta_n$ (a ZGV mode) while the phase velocity $c_n=\omega/\zeta_n$ is non-zero ($n=4$ counting the real branches in Fig. 2a top down).

By now the resonance phenomena associated with backward and ZGV modes in elastic layered waveguides have been well studied and found practical applications [31–34]. However, since, in fluid-loaded guides, the non-attenuating traveling waves turn into leaky waves, the left limit of the backward mode range becomes blurry, and the associated ZGV effects are not so pronounced.

The reason for that difference is evident in the change of trajectories along which the backward-mode poles come from the complex plane to the real axis with increasing frequency (Fig. 3). Such a transformation of complex branches was already noted in Refs. [7,23]. While in a free guide all regular (i.e., non-backward-mode) poles $\pm\,\zeta_n$ enter the real axis through the origin (Fig. 2a), the two ZGV-generic (irregular) complex conjugate poles move toward each other and merge at the real axis in the non-zero double pole $\zeta_n=1.69$ at the ZGV mode frequency $\omega=5.42$ (Fig. 3a). Then they diverge in different directions along the real axis yielding two traveling waves: regular S_1 and backward S_1^* (see also the corresponding branches in Fig. 2a). The positive regular pole of the S_1 mode moves to the right while the pole of the backward wave S_1^* moves to the origin (the negative counterparts $-\zeta_n$ and $-\zeta_n^*$ are centrally symmetric with respect to the origin).

The corresponding deviations of the unfolded integration contour Γ from the real axis, to get around the regular and irregular real poles in accordance with the principle of limiting absorption [27], are shown in Fig. 3c. It should be mentioned that only such a choice of the directions of deviation in the integral representations for the generated wave fields provides wave energy outflow from the source to infinity in an ideally elastic free guide in the backward wave range [27].

Note that a pair of backward mode branch poles ζ_n and $-\zeta_n^*$, e.g., of the modes S_1 and $-S_1^*$ in the example above, always gets into the closed integration contour together unlike a pair of regular poles $\pm\,\zeta_n$, only one of which contributes in GW asymptotics (17). Hence, a pair of poles ζ_n and ζ_n^* obtained from the bending part of a backward mode branch at certain frequency is unbreakable. Its contribution into the GW asymptotics should not be treated as two separate modes. Such a consideration just leads to unexpected seemingly unusual effects.

After the meeting at the origin with the symmetric negative pole, the irregular real pole of the S_1^* mode goes briefly to the imaginary axis and returns through the origin on the real axis at the cut-off frequency $\omega=6.28$. Then it moves to the right, creating now the pure real branch of the S_2 mode (see also Fig. 2a).

With a fluid-loaded plate, the complex poles cease to be exactly

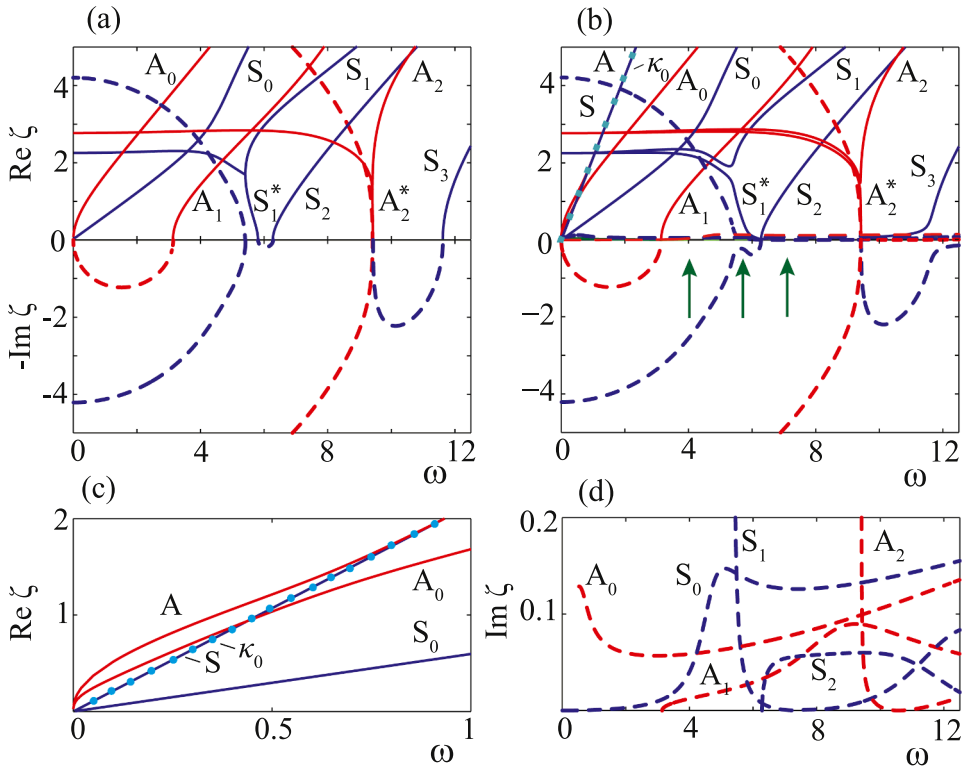

Fig. 2. Real (solid lines) and imaginary (dashed lines) branches of the dispersion curves $\alpha = \zeta_n(\omega)$ for a free (a) and submerged (b) elastic plate; zoomed-in low-frequency range with Scholte-Stoneley modes A and S and A_0 mode crossing the border κ_0 (dotted line) between the domains of real and complex wavenumbers (traveling and leaky waves) (c); imaginary parts of leaky Lamb modes (d) in the submerged plate; within the figure scale, the line κ_0 overlaps the S-mode branch but still not coincide; the asterisks indicate the backward-mode parts of the branches.

complex-conjugate ones (Fig. 3b). They also move toward each other, but the mirror symmetry about the real axis is no longer held (while the central symmetry still holds). They do not reach the real axis but turn apart nearby to the left and to the right, and move along it remaining in the complex plane (leaky GWs). Thus, no classical ZGV mode at a meeting point occurs. And the imaginary part of the pole corresponding to the quasi-backward mode S_1^* is significantly larger in absolute value than that of S_1. This is consistent with the fact that a backward leaky wave decays faster than regular GWs.

After passing the origin, the pole corresponding to the quasi-backward mode S_1^* converts into the pole of regular mode S_2, same as in the free-layer case, with the difference in a slight shift of the pole trajectory into the complex plane. Due to those shifts of the former real poles (Fig. 2d), there is no longer necessity to deviate the integration contour from the real axis to get around the nearly real poles, except the poles associated with the Scholte-Stoneley modes that appear on the real axis (Fig. 3d).

In spite of the absence of classical ZGV modes in a fluid-loaded

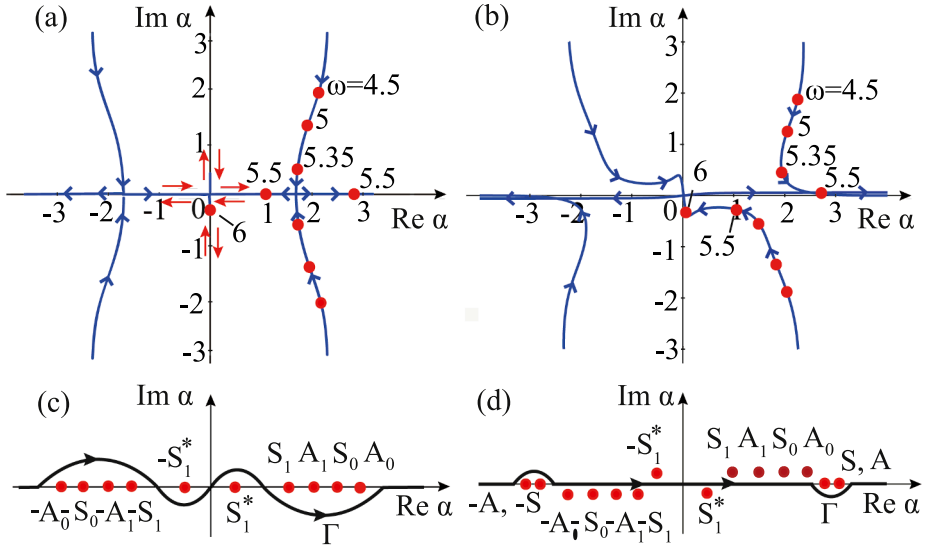

Fig. 3. The trajectories along which the dimensionless complex poles associated with the mode S_1 and the backward mode S_1^* shown in Fig. 2a, b move with increasing frequency in the case of free (a) and water-loaded (b) steel plate; the dots show the poles' location at certain fixed frequencies ω; the corresponding forms of the integration path Γ at $\omega = 5.5$ (in the backward mode range) for the case of free (c) and water-loaded (d) plate.

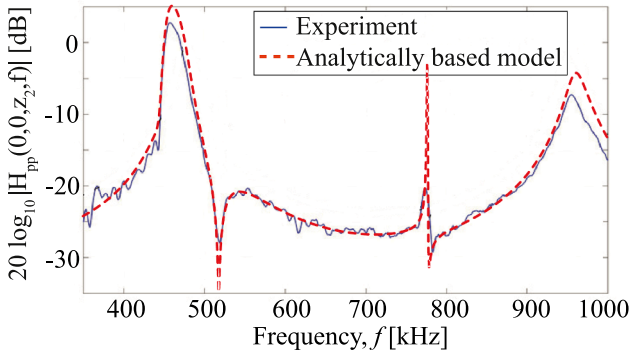

Fig. 4. Experimentally obtained [22] transfer function $|H_{pp}(f)|$ (solid line) and that function calculated within the analytically based model developed (dashed line).

plate, the former ZGV frequencies still manifest themselves in certain resonance effects, such as the effect of increasing acoustic penetration through the plate [21,22,35].

6. Resonance acoustic transparency

To validate the mathematical model developed against experimental and numerical data, we have selected the recent results of Ref. [22], where a resonance sound transmission through a water-immersed steel plate has been experimentally observed and FEM-based simulated. In addition to the validation goals, the results obtained give an insight into the mechanism of the resonance transmission observed.

The transmission of time-harmonic acoustic waves through the plate is characterized by the pressure-to-pressure transfer function $H_{pp} = p(\mathbf{x}_2)/p(\mathbf{x}_1)$, where points $\mathbf{x}_1$ and $\mathbf{x}_2$ are taken on the top plate surface and in the liquid under the plate, respectively. Fig. 4 gives an example of the experimentally obtained [22] (solid line) and analytically based simulated (dashed line) transfer function H_{pp} for the transducer of radius $a = 30$ mm located at the distance $d = 270$ mm above the plate; point $\mathbf{x}_2$ is located 100 mm below the plate. One can see a good coincidence of these experimental and theoretical results as well as the results of FEM calculations that was also presented in Ref. [22].

Fig. 5 gives one more validating example. It presents spatial patterns of the acoustic pressure magnitudes generated in the same structure as in the previous example at the frequencies $f = 457$ and 956 kHz at which the peaks of acoustic transfer through the plate occur. For comparability, the coordinate system is the same as in Ref. [22], from which the images (a) and (b) are copied. They were calculated using the finite element-angular spectrum method (FEM-ASM) while the bottom pictures (c) and (d) display the results obtained using the integral and asymptotic representations. The patterns in the top and bottom images are similar. The difference in magnitudes is due to different source models: FEM simulation of the in-house-constructed transducer [22] (a, b) versus the uniform dimensionless distribution ($q_0 = 1$) in the circular area $r < a$ (c, d). Specific integral representations of the pressure fields $p_{sc}^{\pm}$ derived for such a source are given in Appendix A.

It should be mentioned that only the source field p_0 is shown above the plate in Fig. 5, same as in Ref. [22], while the full field in the upper half-space includes the reflection pressure field p_{sc}^{-} as well. Accounting for the latter drastically changes the pressure pattern above the plate. The beams, reflected from the plate are superimposed on the beams emanated from the transducer creating a lattice pattern (Fig. 6). The images (a), (b), and (c) of Fig. 6 are for the frequencies $f = 329$, 457, and 576 (kHz) taken close before, inside, and just after the former backward-mode range; the corresponding dimensionless frequencies $\omega = 4$, 5.5, and 7 are indicated in Fig. 2b by arrows. Fig. 6 is intended to illustrate the increased acoustic energy transfer in the vicinity of the former ZGV-mode frequency. Indeed, one can see that the vertical beams penetrating through the plate at non-resonance frequencies 329 kHz and 576 kHz ($\omega = 4$ and 7) look much weaker than that in the central subplot.

The patterns of acoustic pressure in Figs. 5 and 6 give an idea of the spatial distribution of acoustic power while specific trajectories of time-averaged energy transfer in a time-harmonic wave field can be visualized by energy streamlines that are tangential to the Umov-Poynting vectors of energy flux intensity $\mathbf{e}$ at each point [31,34,36,37]. Fig. 7 depicts the streamline structures for the pressure fields shown in Fig. 6a, b. The bottom zoomed-in insets (c) and (d) of Fig. 7 are for the

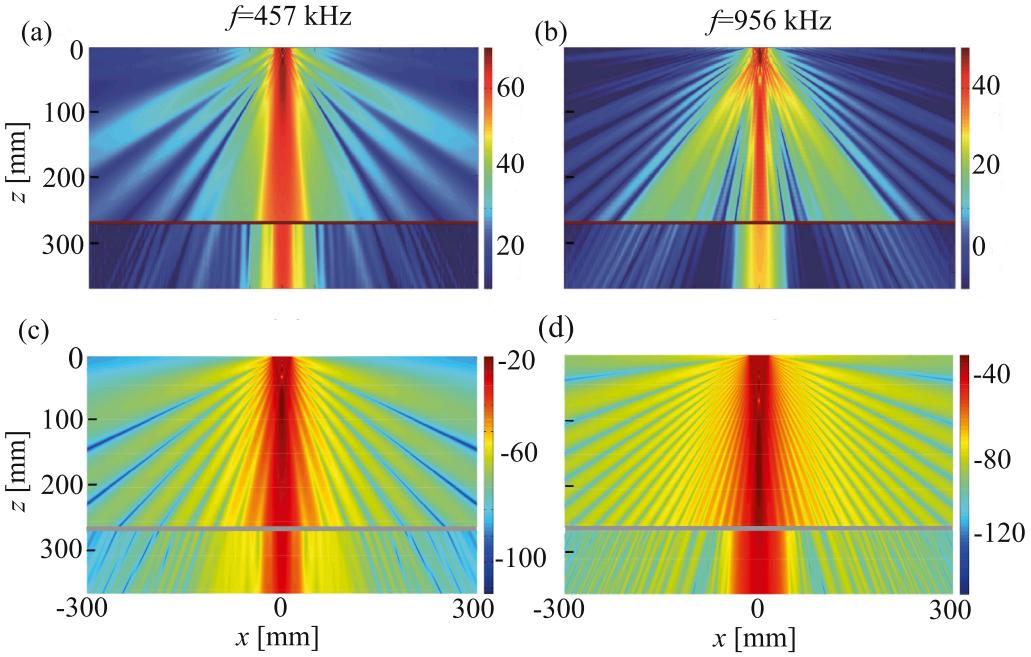

Fig. 5. Patterns of transducer-generated and transmitted pressure magnitudes ($20\log_{10}|p_0|$ for $z > 0$ and $20\log_{10}|p_{sc}^{+}|$ for $z < -h$ [dB re 1 Pa/Hz]) calculated by FEM-ASM [22] (a, b) and the magnitudes $20\log_{10}|p_0/p_u|$ for $z > 0$ and $20\log_{10}|p_{sc}^{+}/p_u|$ for $z < -h$ calculated within the analytically based model for the source simulated by the dimensionless distribution $q_0 = 1$ (c, d).

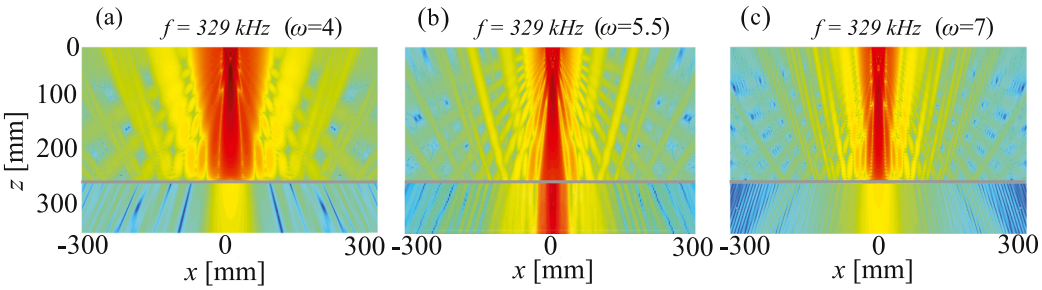

Fig. 6. Full-field pressure patterns for the frequencies taken close before, inside, and just after the backward-mode range illustrating increased acoustic penetration at the backward-mode frequency.

streamlines inside the plate. Their patterns can visually explain the increase in the energy transfer through the plate at the resonance frequency.

In the regular case ($\omega = 4, f = 329$ kHz), only a few close to the central axis streamlines go directly through the plate (Fig. 7a, c). The others either turn upward being reflected from the plate or turn laterally depicting winding trajectories of energy transfer along the plate with the excited GWs. These sinuous streamlines regularly approach the horizontal boundaries of the plate, and small portions of energy are re-radiated into the liquid feeding the reflected and transmitted fields $p_{sc}^{\pm}$ in the course of leaky GW propagation.

In the resonance case ($\omega = 5.5, f = 457$ kHz), the streamlines inside the plate are featured by the appearance of energy vortices that essentially change the regular pattern of wavy lateral energy flow along the plate. Much more streams blocked by the lateral vortices [38] go down into the lower liquid half-space, thus, increasing the acoustic transfer.

7. Energy transfer

The time-averaged over the period of oscillation amount of wave energy transferred in a time-harmonic elastic or acoustic wave field through a surface S is specified by the quantity [20]

$$E = \int\int_S e_s(\mathbf{x})dS, \quad e_s = -\frac{\omega}{2}\mathrm{Im}\left(\mathbf{u}, \tau_s\right), \tag{18}$$

where $e_s = (\mathbf{e}, \mathbf{n})$ is the projection of the Umov-Poynting vector $\mathbf{e}$ onto the surface normal $\mathbf{n}$;τ_s is the stress vector at a surface element with the normal $\mathbf{n}$; the scalar product of complex vectors assumes complex conjugate components of the second multiplier.

In such particular cases of surface S as a closed surface around the source, horizontal planes $z = \text{const}$ far above the source and far below the plate, and a lateral cylindrical surface $r = \text{const}$ of large radius r, Eq. (17) yields the source energy E_0, the energy the reflected and transmitted waves E^- and E^+, and the lateral energy outflow to infinity with GWs E_r. A detailed description of the derivation of specific expressions for E_0, $E^{\pm}$ and E_r in terms of Green's functions and surface stress $\mathbf{q}$ is available in [34] and papers cites therein.

Using this technique, similar expressions for the case under consideration have been derived and tested [39]. The main criterion was the fulfilment of the energy balance

$$E_0 = E^- + E^+ + E_r$$

in the entire frequency range of interest, including the leaky backward mode band. In the present paper, we focus on the energy transfer by guided waves, including seemingly unusual energy properties of leaky backward waves discussed in Ref. [24]. The unusualness is associated with the opposite directions of the horizontal components of wave energy fluxes in different parts of the vertical energy-flux profile of the backward leaky wave, which is schematically illustrated in Fig. 4 of Ref. [24]. In fact, this behavior is not quite unusual, and it does not violate the energy balance.

The occurrence of energy flux density vectors $\mathbf{e}(\mathbf{x}) = (e_r, e_z)$ directed back to the source does not mean that the backward energy flux goes up to the source. If this occurs in the vertical energy profile $e_r(z)$ of a separate mode, this may not occur in the total wave field consisting of the sum of normal modes and bulk waves. Their interference completely

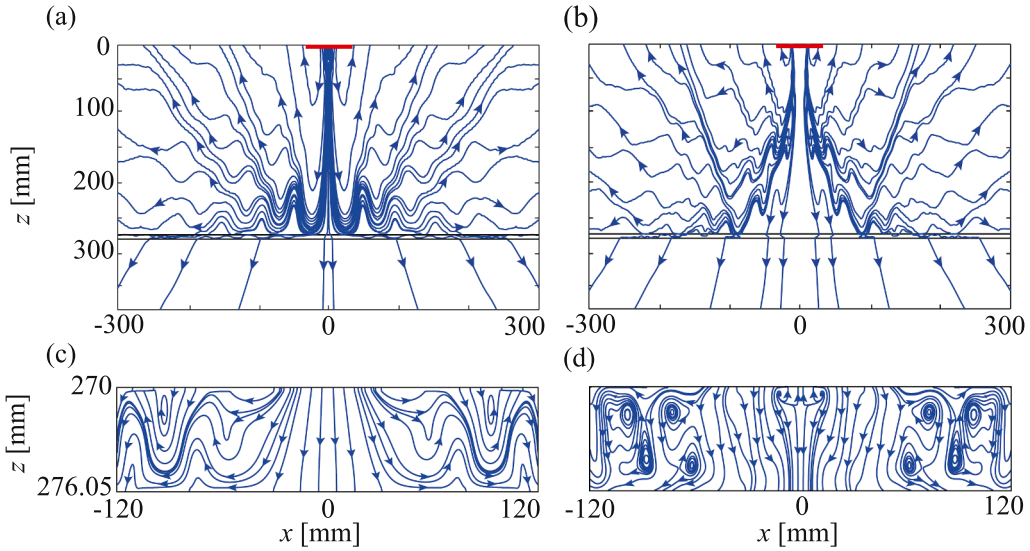

Fig. 7. Energy streamlines in the same time-harmonic fields as in Fig. 6a and b (a, b), thick horizontal segments at the top show the size of the emitter; bottom insets (c, d) show streamlines in the vertically zoomed-in plate domain D.

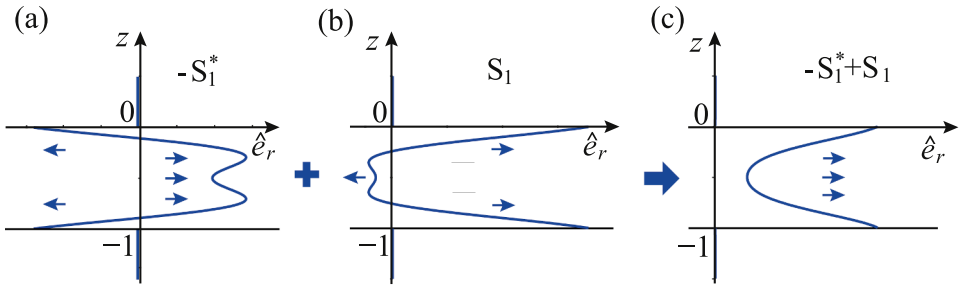

Fig. 8. Dimensionless normalized profiles $\hat{e}_r(z)$ of energy fluxes associated with each of the modes $-S_1^*$ and S_1 separately (a, b) and the profile of their sum (c); $\omega = 5.5$.

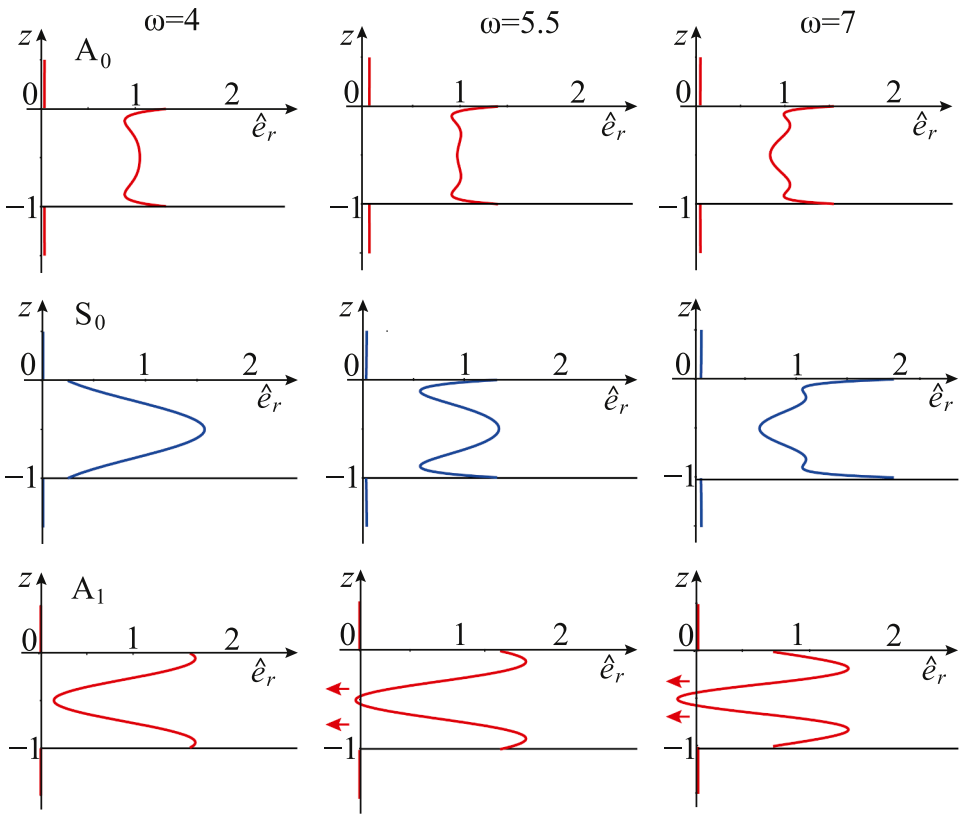

Fig. 9. Examples of energy-flux profiles $\hat{e}_r(z)$ of the regular Lamb modes A_0, S_0 and A_1 (top, central, and bottom rows of subplots) at dimensionless frequencies $\omega = 4$, 5.5, and 7 (left, central, and right columns).

changes the pattern of the vector field $\mathbf{e}(\mathbf{x})$ in comparison with x-independent profiles of single traveling waves. In the total field, the backward vectors $\mathbf{e}$ usually indicates the appearance of energy vortices, i.e., spatial areas in which the time-averaged energy circulates along closed paths without inflow or outflow [31,40,41]. The total energy flux through any cross-section of the vortex area is equal to zero; therefore, they cannot violate the energy balance.

In rare cases, backward energy flows coming from infinity can arise in ideally elastic waveguides. But, in the near field, such an inverse stream is necessarily turned away by the more powerful energy flux from the source. Mathematically, the turn is due to the evanescent modes associated with the complex ζ_n. Their contribution to the total field is negligible at a distance from the source, but they come into play in the near field. Numerical examples of such backward energy fluxes from infinity are presented in Refs. [31,34]. Those backflows can be treated as sleeves of vortices circulated through infinity, and they also violate neither energy balance nor the condition of energy radiation to infinity.

Moreover, although the energy profiles $e_r(z)$ of backward modes typically exhibit opposite direction at various depths z (e.g., Fig. 8a, b), they are, as noted above, unbreakable. They always enter the total field together, and the profile of their summary contribution is already directed from the source (Fig. 8c).

For convenience, Figs. 8–10 display normalized profiles of leaky modes $\hat{e}_r(z) = \lim_{r\to\infty} e_r(z) r e^{2\mathrm{Im}\zeta_n r}$, non-decreasing as $r \to \infty$. In these figures, they are shown as vertical plots of the dimensionless coordinate $z := z/h$. The plate cross-section is $-1 \leqslant z \leqslant 0$while $z \geqslant 0$and $z \leqslant -1$are for the fluid environment. In the latter, the horizontal energy flux is comparatively weak (except for the Scholte-Stoneley modes in Fig. 10), and the plots of $\hat{e}_r(z)$ in these domains look as vertical lines closely pressed to the axis z.

The energy-flux profiles of regular Lamb modes are typically without negative sections (Fig. 9). Although, sometimes such behavior also occurs (e.g., the profile of A_1 mode at $\omega = 5.5$ and 7).

It should not be forgotten that the backward energy streams coming from infinity occur only in the fields of traveling guided waves associated with purely real wavenumbers ζ_n. Since in an immersed plate all the Lamb waves, except the low-frequency A_0 mode, become leaky GWs

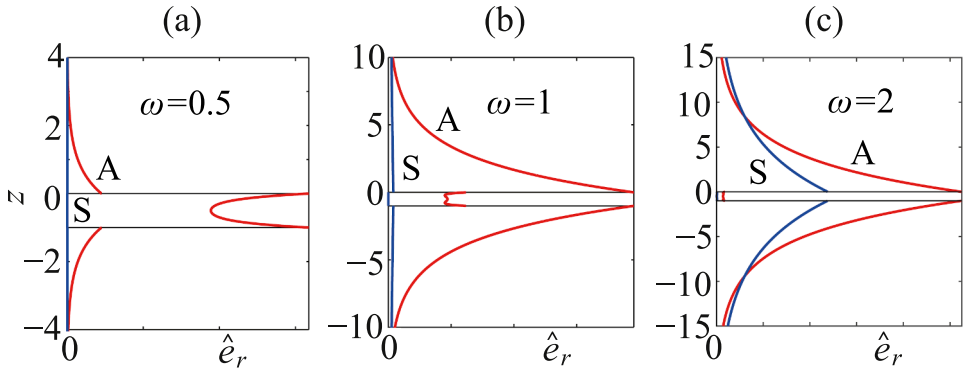

Fig. 10. Energy-flux profiles of the Scholte-Stoneley modes *A* and *S*.

with complex wavenumbers, they decay exponentially as the distance *r* increases without the possibility of delivering energy to infinity. Respectively, no backward fluxes from infinity may exist with leaky modes, and all vortex phenomena may only occur in the middle and near field.

Besides the mode A_0, which wavenumber, however, is real only at low frequencies, far from the backward mode band, the only GWs with purely real wavenumbers in the whole frequency range are Scholte-Stoneley modes *A* and *S*. They provide the delivery of wave energy to infinity along the plate, but their profiles do not assume backward fluxes (Fig. 10). As an illustration of the *A* and *S* mode contribution into the total energy transfer to infinity, Fig. 11 shows the dimensionless frequency dependencies of the full source power $E_0(\omega)$ of the monopole source located near the plate ($d = h$), and its partition among the reflected and transmitted bulk waves ($E^{\pm}$) and *A* and *S* guided waves. The circular markers are for the sum $E_r + E^- + E^+$to confirm the energy balance (in the range $\omega > 0.44$, $E_r = E_A + E_S$).

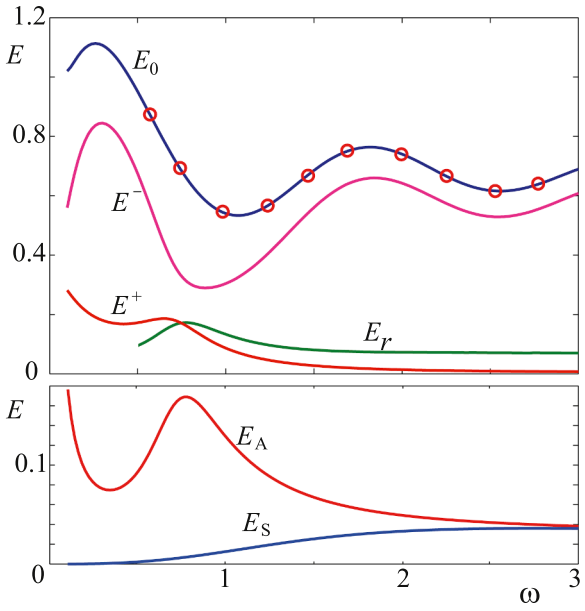

Fig. 11. Frequency dependence of the point source power E_0 and its partition among the reflected, transmitted and non-attenuating guided waves *A* and *S* (E^-, E^+, and E_r, respectively, circular markers are for their sum, top subplot); partition of the guided wave energy E_r between the *A* and *S* modes (bottom).

8. Conclusions

The analytically based computer model for the ultrasonic sounding of a fluid-loaded elastic plate has been developed on the basis of explicit integral and asymptotic representations for the Green's function of the coupled acoustic-elastic structure. The analysis of the source energy spatial distribution and the visualization of wave energy fluxes in the total wave field help to clarify the mechanism of the resonant acoustic transparency of the plate and energy properties of leaky backward modes, which seemed to be unusual. The model has been validated against FEM and experimental results only for isotropic plates, but the existing algorithms of Green's matrix calculation for anisotropic, functionally graded and laminate structures make it possible to use the model with a wider range of plate samples of complex structure (composite materials).

Acknowledgements

The work is supported by the Russian Science Foundation (Project No. 17-11-01191).

Appendix A

In the case of an isotropic plate and axially symmetric source function q_0 distributed in a circular domain $0 \leqslant r \leqslant a$, which is parallel to the plate surface $z = 0$ and located above it at the distance d ($\zeta = d$), the axisymmetric fields $p_{sc}^{\pm}$ and $\mathbf{u} = (u_r, u_z)$ can be represented in terms of onefold path integrals

$$p_{sc}^{-}\left(r, z\right) = \frac{1}{2\pi}\int_{\Gamma_+} G_{sc}^{-}\left(\alpha, z; d\right) Q_0(\alpha) J_0\left(\alpha r\right) \alpha d\alpha, \quad z \geqslant 0,$$

$$u_r\left(r, z\right) = \frac{1}{2\pi}\int_{\Gamma_+} S\left(\alpha, z\right) Q\left(\alpha, d\right) Q_0(\alpha) J_1\left(\alpha r\right) \alpha^2 d\alpha, \quad -h \leqslant z \leqslant 0,$$

$$u_z\left(r, z\right) = \frac{1}{2\pi}\int_{\Gamma_+} R\left(\alpha, z\right) Q\left(\alpha, d\right) Q_0(\alpha) J_0\left(\alpha r\right) \alpha d\alpha, \quad -h \leqslant z \leqslant 0,$$

$$p_{sc}^{+}\left(r, z\right) = \frac{1}{2\pi}\int_{\Gamma_+} G_{sc}^{+}\left(\alpha, z; d\right) Q_0(\alpha) J_0\left(\alpha r\right) \alpha d\alpha, \quad z \leqslant -h.$$

Here Γ_+ is the right half of the contour Γ (Fig. 3d),

$$G_{sc}^{-} = -(\sigma_0\Delta + \rho_0\omega^2\widehat{R}(\alpha, 0))e^{-\sigma_0(z+d)}/(2\sigma_0\Delta_0)$$
$$G_{sc}^{+} = -\rho_0\omega^2\sigma_0\widehat{R}(\alpha, z)e^{-\sigma_0 d}/\Delta_0$$
$$\Delta_0 = \sigma_0\Delta - \rho_0\omega^2\widehat{R}(\alpha, 0)$$

$\widehat{R}, \widehat{S}$ are the constituents of the third column $\mathbf{K}_3$ of the half-space Green's matrix K:

$$\mathbf{K}_3 = (-i\alpha_1\widehat{S}, -i\alpha_2\widehat{S}, \widehat{R}),$$

which are also in the integrands for the radial and vertical displacement components u_r and u_z:

$$S(\alpha, z) = \widehat{S}(\alpha, z)/\Delta, \quad R(\alpha, z) = \widehat{R}(\alpha, z)/\Delta$$

$$\widehat{S} = (S_1\Delta - \rho_0\omega^2 R_{1,h}S_2)/\Delta_L, \quad \widehat{R} = (R_1\Delta - \rho_0\omega^2 R_{1,h}R_2)/\Delta_L, \quad -h \leqslant z \leqslant 0$$

$$\Delta = \sigma_0\Delta_L + \rho_0\omega^2 R_{2,h}, \quad R_{n,h} = R_n(\alpha, -h), \quad n = 1, 2$$

$$S_1(\alpha, z) = -i[\sigma_{12}(\alpha^2\gamma^2c_2 + \gamma^4c_1) - \sigma_{12}\gamma^4cc_{21} + \alpha^2\sigma_{12}^2ss_{21} - \alpha^2\sigma_{12}\gamma^2cc_{12} + \gamma^6ss_{12}]$$
$$R_1(\alpha, z) = \sigma_1[-\alpha^2(\sigma_{12}\gamma^2s_1 + \gamma^4s_2) + \alpha^2\sigma_{12}\gamma^2cs_{21} - \gamma^6sc_{21} + \alpha^2\gamma^4cs_{12} - \alpha^4\sigma_{12}sc_{12}]$$
$$S_2(\alpha, z) = S_1(\alpha, -z-h), \quad R_2(\alpha, z) = R(\alpha, -z-h)$$
$$\Delta_L = 2\mu[-2\alpha^2\sigma_{12}\gamma^4 - (\gamma^8 + \alpha^4\sigma_{12})s_1(h)s_2(h) + 2\alpha^2\sigma_{12}\gamma^4c_1(h)c_2(h)]$$

$$\sigma_{12} = \sigma_1\sigma_2, \quad s_n(z) = \mathrm{sh}(\sigma_n z), \quad c_n(z) = \mathrm{ch}(\sigma_n z)$$
$$ss_{mn}(z) = s_m(z)s_n(z+h), \quad cc_{mn}(z) = c_n(z)c_m(z+h)$$
$$sc_{mn}(z) = s_m(z)c_n(z+h), \quad cs_{mn}(z) = c_m(z)s_n(z+h), \quad m, n = 1, 2$$
$$\gamma^2 = \alpha^2 - \kappa_2^2/2, \quad \sigma_n = \sqrt{\alpha^2 - \kappa_n^2}, \quad \kappa_0 = \omega/c_0, \quad \kappa_1 = \omega/c_p, \quad \kappa_2 = \omega/c_s$$

$$Q(\alpha, \zeta) = -(\Delta/\Delta_0)e^{-\sigma_0\zeta}$$
$$Q_0(\alpha) = 2\pi\int_0^a q_0(r)J_(\alpha r)rdr = 2\pi a J_1(a\alpha)/\alpha \text{ for } q_0 = 1$$

J_0 and J_1 are the Bessel functions.

Appendix B. Supplementary material

Supplementary data associated with this article can be found, in the online version, at https://doi.org/10.1016/j.ultras.2018.10.001.

References

[1] W.A. Grandia, C.M. Fortunko, NDE applications of air-coupled ultrasonic transducers, IEEE Ultrasonic Symposium, Proceedings, vol. 1, 1995, pp. 697–709.
[2] V. Giurgiutiu, Structural Health Monitoring with Piezoelectric Wafer Active Sensors, second ed., Academic Press, New York, 2014.
[3] W. Hillger, D. Ilse, L. Bühling, Lamb-waves for air-coupled ultrasonic testing with one-sided access, in: 8th European Workshop on Structural Health Monitoring (EWSHM 2016), Bilbao, Spain, 2016. < www.ndt.net/app.EWSHM2016 > .
[4] L.M. Brekhovskikh, Waves in Layered Media, second ed., Academic Press, New York, 1980.
[5] M.J. Anderson, P.R. Martin, C.M. Fortunko, Resonant transmission of a three-dimensional acoustic sound beam through a solid plate in air. Theory and measurement, J. Acoust. Soc. Am. 98 (1995) 2628–2638, https://doi.org/10.1121/1.413229.
[6] V.M. Babich, V.S. Buldyrev, Short-Wavelength Diffraction Theory: Asymptotic Methods, Springer-Verlag, Berlin, 1991.
[7] S.I. Rokhlin, D.E. Chimenti, A.H. Nayfeh, On the topology of the complex wave spectrum in a fluid-coupled elastic layer, J. Acoust. Soc. Am. 85 (3) (1989) 1074–1080, https://doi.org/10.1121/1.397490.
[8] A.L. Shuvalov, O. Poncelet, M. Deschamps, Analysis of the dispersion spectrum of fluid-loaded anisotropic plates: leaky-wave branches, J. Sound Vib. 296 (2006) 494–517, https://doi.org/10.1016/j.jsv.2005.12.059.
[9] W. Ke, M. Castaings, C. Bacon, 3D finite element simulations of an air-coupled ultrasonic NDT system, NDT & E Int. 42 (6) (2009) 524–533, https://doi.org/10.1016/j.ndteint.2009.03.002.
[10] S. Banerjee, T. Kundu, Ultrasonic field modeling in plates immersed in fluid, Int. J. Solids Struct. 44 (18–19) (2007) 6013–6029, https://doi.org/10.1016/j.ijsolstr.2007.02.011.
[11] P. Wilcox, R. Monkhoue, M. Lowe, P. Cawley, The use of Huygens' principle to model the acoustic field from interdigital Lamb wave transducers, Annual Review of Progress in Quantitative Nondestructive Evaluation, 1998, pp. 915–922.
[12] L.W. Schmerr, H.-J. Kim, R. Huang, A. Sedov, Multi-Gaussian ultrasonic beam modeling, Proceedings of the World Congress of Ultrasonics, 2003, pp. 93–99.
[13] M. Spies, Analytical methods for modeling of ultrasonic nondestructive testing of anisotropic media, Ultrasonics 42 (2009) 213–219.
[14] D. Placko, T. Kundu, T. Kundu (Ed.), Ultrasonic Nondestructive Evaluation: Engineering and Biological Material Characterization, CRC Press, Boca Raton, FL, 2003, pp. 144–202.
[15] Ye.V. Glushkov, N.V. Glushkova, A.A. Yeremin, V.V. Mikhas'kiv, The layered element method in the dynamic theory of elasticity, J. Appl. Math. Mech. 73 (2009) 449–456, https://doi.org/10.1016/j.jappmathmech.2009.08.005.
[16] Ch.G. Xu, B.Q. Xu, G.D. Xu, Laser-induced thermoelastic Leaky Lamb waves at the fluid-solid interface, Appl. Phys. A 105 (2011) 379–386.
[17] E.V. Glushkov, N.V. Glushkova, S.I. Fomenko, C. Zhang, Surface waves in materials with functionally gradient coatings, Acoust. Phys. 58 (3) (2012) 339–353.
[18] E.V. Glushkov, N.V. Glushkova, A.A. Eremin, Forced wave propagation and energy distribution in anisotropic laminate composites, J. Acoust. Soc. Am. 129 (5) (2011) 2923–2934, https://doi.org/10.1121/1.3559699.
[19] E. Glushkov, N. Glushkova, Ch. Zhang, Surface and pseudo-surface acoustic waves piezoelectrically excited in diamond-based structures, J. Appl. Phys. 112 (2012) 064911.
[20] N.A. Umov, Selected Works, State Publishing House of Technical-Theoretical Literature, Moscow, Russia, 1950, pp. 151–226 (in Russian).
[21] R.W. Boyle, D.K. Froman, I. Reflection of sound energy and thickness of plate reflector-ultrasonic method, Can. J. Res. 1 (5) (1929) 405–424.
[22] M. Aanes, K.D. Lohne, P. Lunde, M. Vestrheim, Beam diffraction effects in sound transmission of a fluid-embedded viscoelastic plate at normal incidence, J. Acoust. Soc. Am. 140 (2016) EL67, https://doi.org/10.1121/1.4954893.
[23] F. Simonetti, M.J.S. Lowe, On the meaning of Lamb mode nonpropagating branches, J. Acoust. Soc. Am. 118 (2005) 186–192.
[24] I.A. Nedospasov, V.G. Mozhaev, I.E. Kuznetsova, Unusual energy properties of leaky backward Lamb waves in a submerged plate, Ultrasonics 135 (2017) 95–99, https://doi.org/10.1016/j.ultras.2017.01.025.
[25] E. Dieulesaint, D. Royer, Elastic Waves in Solids: Applications to Signal Processing, Chichester [Eng.], Wiley, New York, 1980.
[26] A.G. Sveshnikov, Limiting absorption principle for a waveguide, Dokl. Akad. Nauk SSSR 80 (3) (1951) 341–344 (in Russian).
[27] I.I. Vorovich, V.A. Babeshko, Dynamic Mixed Problems of Elasticity for Nonclassical Domains, Nauka, Moscow, 1974 (in Russian).
[28] E.V. Glushkov, N.V. Glushkova, O.A. Miakisheva, The interaction of sound and ultrasound waves with multilayered elastic plates immersed in acoustic fluid, Days on Diffraction 2015, 2015, pp. 107–111, , https://doi.org/10.1109/DD.2016.7756835.
[29] M.F.M. Osborne, S.D. Hart, Transmission, reflection, and guiding of an exponential

pulse by a steel plate in water. I. Theory, J. Acoust. Soc. Am. 17 (1) (1945) 1–18, https://doi.org/10.1121/1.1916293.
[30] J.-P. Sessarego, J. Sagéloli, C. Gazanhes, H. Überall, Two Scholte – Stoneley waves on doubly fluid-loaded plates and shells, J. Acoust. Soc. Am. 101 (1) (1997) 135–142, https://doi.org/10.1121/1.418014.
[31] V.A. Babeshko, E.V. Glushkov, N.V. Glushkova, Energy vortices and backward fluxes in elastic waveguides, Wave Motion 16 (3) (1992) 183–192, https://doi.org/10.1016/0165-2125(92)90027-Y.
[32] C. Prada, D. Clorennec, D. Royer, Local vibration of an elastic plate and zero-group velocity Lamb modes, J. Acoust. Soc. Am. 124 (1) (2008) 203–212, https://doi.org/10.1121/1.2918543.
[33] C. Prada, D. Clorennec, T.W. Murray, D. Royer, Influence of the anisotropy on zero-group velocity Lamb modes, J. Acoust. Soc. Am. 126 (2) (2009) 620–625, https://doi.org/10.1121/1.3167277.
[34] E.V. Glushkov, N.V. Glushkova, S.I. Fomenko, Wave energy transfer in elastic half-spaces with soft interlayers, J. Acoust. Soc. Am. 137 (4) (2015) 1802–1812, https://doi.org/10.1121/1.4916607.
[35] M. Michaud, T. Leong, P. Swiergon, P. Juliano, K. Knoerzer, Design parameters of stainless steel plates for maximizing high frequency ultrasound wave transmission, Ultrason. Sonochem. 26 (2015) 56–63, https://doi.org/10.1016/j.ultsonch.2015.01.007.
[36] D.M.F. Chapman, Using streamlines to visualize acoustic energy flow across boundaries, J. Acoust. Soc. Am. 124 (1) (2008) 48–56, https://doi.org/10.1121/1.2931956.
[37] E.V. Glushkov, N.V. Glushkova, O.A. Godin, The effect of anomalous transparency of the water – air interface for a volumetric sound source, Acoust. Phys. 59 (1) (2013) 8–18, https://doi.org/10.1134/S106377101206005X.
[38] E.V. Glushkov, N.V. Glushkova, Blocking property of energy vortices in elastic waveguides, J. Acoust. Soc. Am. 102 (3) (1997) 1356–1360, https://doi.org/10.1121/1.420054.
[39] E.V. Glushkov, N.V. Glushkova, O.A. Miakisheva, Guided wave generation and source energy partition in acoustic fluid with an immersed elastic plate, Days on Diffraction 2016, 2016, pp. 166–170, , https://doi.org/10.1109/DD.2016.7756835.
[40] V.A. Babeshko, E.V. Glushkov, N.V. Glushkova, Analysis of wave fields generated in a stratified elastic half-space by surface sources, Sov. Phys. Acoust. 32 (3) (1986) 223–226.
[41] R.V. Waterhouse, D.G. Crighton, J.E. Ffowcs-Williams, A criterion for an energy vortex in a sound field, J. Acoust. Soc. Am. 81 (5) (1987) 1323–1326, https://doi.org/10.1121/1.394537.